

Ring-bursting behavior en route to turbulence in narrow-gap Taylor-Couette flowsSebastian Altmeyer,^{1,*} Younghae Do,^{2,†} and Ying-Cheng Lai³¹*Institute of Science and Technology Austria, 3400 Klosterneuburg, Austria*²*Department of Mathematics, KNU-Center for Nonlinear Dynamics, Kyungpook National University, Daegu, 702-701, Korea*³*School of Electrical, Computer and Energy Engineering, Arizona State University, Tempe, Arizona 85287, USA*

(Received 9 November 2014; revised manuscript received 22 October 2015; published 24 November 2015)

We investigate the Taylor-Couette system where the radius ratio is close to unity. Systematically increasing the Reynolds number, we observe a number of previously known transitions, such as one from the classical Taylor vortex flow (TVF) to wavy vortex flow (WVF) and the transition to fully developed turbulence. Prior to the onset of turbulence, we observe intermittent bursting patterns of localized turbulent patches, confirming the experimentally observed pattern of very short wavelength bursts (VSWBs). A striking finding is that, for a Reynolds number larger than that for the onset of VSWBs, a new type of intermittently bursting behavior emerges: patterns of azimuthally closed rings of various orders. We call them *ring-bursting* patterns, which surround the cylinder completely but remain localized and separated in the axial direction through nonturbulent wavy structures. We employ a number of quantitative measures including the cross-flow energy to characterize the ring-bursting patterns and to distinguish them from the background flow. These patterns are interesting because they do not occur in the wide-gap Taylor-Couette flow systems. The narrow-gap regime is less studied but certainly deserves further attention to gain deeper insights into complex flow dynamics in fluids.

DOI: [10.1103/PhysRevE.92.053018](https://doi.org/10.1103/PhysRevE.92.053018)

PACS number(s): 47.20.Ky, 47.32.cf, 47.54.-r

I. INTRODUCTION

Turbulence is arguably one of the most difficult problems in science and engineering. The vast literature in this field [1] has mostly focused on fully developed turbulence. The purpose of this paper is to report a phenomenon of intermittency associated with the evolution of turbulence in a prototypical model system of shear flow: the Taylor-Couette system [2] with the gap between the inner and outer cylinders so narrow that flow is effectively a curved Couette flow. This type of intermittency occurs *en route* to turbulence as the Reynolds number is increased which, to our knowledge, has not been reported previously.

The Taylor-Couette system, a flow between two concentric rotating cylinders, has been a paradigm in the study of complex dynamical behaviors of fluid flows, especially turbulence [3–11]. The flow system can exhibit a large variety of ordered and disordered behaviors in different parameter regimes. The parameters that control the system dynamics include the values of the rotation speed of the inner and outer cylinders, as well as their radius ratio. Most previous studies have dealt with the setting in which the radius ratio is below, say, about 0.95, the so-called wide-gap regime [6]. The primary interest of this work is in the *narrow-gap* case, where the radius ratio is close to unity. We fix the radius ratio to be 0.99. While different configurations of rotation of the inner and outer cylinders can lead to distinct dynamical behaviors, to be concrete we restrict our study to the case in which the outer cylinder is stationary. In fact, regardless of whether the outer cylinder is rotational or stationary, transition to turbulence can occur as the Reynolds number is increased. For different system and parameter settings, there can be distinct routes to turbulence. For example, for systems of counter-rotating cylinders, an

early work [3] showed that transition to turbulence can be sudden as the Reynolds number is increased through a critical point. For a stationary outer cylinder, the transition from laminar flow to turbulence can occur through a sequence of instabilities of distinct nature [10,12].

For the Taylor-Couette system of counter-rotating cylinders, spatially isolated flow patterns such as localized patches can emerge and decay through the whole fluid domain [6,13]. Depending on the parameters, the localized patches can be laminar or exhibit more complex patterns such as interpenetrating spirals [6]. In the wide-gap regime, numerical simulations [14] revealed the existence of the Görtler vortices [15], which are small-scale azimuthal vortices that can cause streaky structures and form herringbone-like patterns near the wall. Localized turbulent behaviors can arise when the Görtler vortices concentrate and grow at the outflow boundaries of the Taylor vortex cell [14].

For narrow-gap flows, there was experimental evidence of the phenomenon of very short wavelength bursts (VSWBs) [10]. One contribution of our work is an explicit computational demonstration of VSWBs. Remarkably, we uncover a class of solutions *en route* to turbulence. These are localized, irregular, intermittently bursting, azimuthally closed patterns that manifest themselves as various rings located along the axial direction. For convenience, we refer to the states as “*ring bursts*.” Depending on the parameter setting, the number of distinct rings can vary, but their extents in the axial direction are similar. The ring bursts can occur on some background flow that is not necessarily regular. For example, in a typical setting the background can be wavy vortex flows (WVFs) with relatively high azimuthal wave numbers. Because of the coexistence of complex flow patterns, to single out ring bursts is challenging, a task that we accomplish by developing an effective azimuthal wave number separation method based on the cross-flow energy. We also find that ring bursts are precursors to turbulence, *signifying a new route to turbulence* uniquely for narrow-gap Taylor-Couette flows. To

*sebastian.altmeyer@ist.ac.at

†yhdo@knu.ac.kr

our knowledge, there has been no prior report of ring-bursting patterns or similar phenomena. This is mainly due to the fact that this narrow-gap regime is a less explored territory in the giant landscape of turbulence research. It would be interesting to identify precursors to turbulence in flow systems in general.

In Sec. II, we outline our numerical method and describe a number of regular states in our narrow-gap Taylor-Couette system. In Sec. III, we present our main results: numerical confirmation of experimentally observed VSWBs and, more importantly, identification and quantitative confirmation of intermittent ring bursts as precursors to turbulence. In Sec. IV, we present conclusions and discussions.

II. NUMERICAL METHOD AND BASIC DYNAMICAL STATES OF NARROW-GAP TAYLOR-COUPETTE FLOW

A. Numerical method

The Taylor-Couette system consists of two independently rotating cylinders of finite length L and a fluid confined in the annular gap between the two cylinders. We consider the setting in which the inner cylinder of radius R_i rotates at angular speed Ω and the outer cylinder of radius R_o is stationary. The end walls enclosing the annulus in the axial direction are stationary and the fluid in the annulus is assumed to be Newtonian, isothermal, and incompressible with kinematic viscosity ν . Using the gap width $d = R_o - R_i$ as the length scale and the radial diffusion time d^2/ν as the time scale, the nondimensionalized Navier-Stokes and continuity equations are

$$\partial_t \mathbf{u} + (\mathbf{u} \cdot \nabla) \mathbf{u} = -\nabla p + \nabla^2 \mathbf{u}, \quad \nabla \cdot \mathbf{u} = 0, \quad (1)$$

where $\mathbf{u} = (u_r, u_\theta, u_z)$ is the flow velocity field in the cylindrical coordinates (r, θ, z) , the corresponding vorticity is given by $\nabla \times \mathbf{u} = (\xi, \eta, \zeta)$, and r is the radius of the fluid domain in the gap ($r_i \leq r \leq r_o$). The three relevant parameters are the Reynolds number $\text{Re} = \Omega_i R_i d / \nu$, the radius ratio $R_i / R_o = 0.99$, and the aspect ratio $\Gamma \equiv L/d = 44$. The boundary conditions on the cylindrical surfaces are of the no-slip type, with

$$\mathbf{u}(r_i, \theta, z, t) = (0, Re, 0), \quad \mathbf{u}(r_o, \theta, z, t) = (0, 0, 0), \quad (2)$$

where the nondimensionalized inner and outer radii are $r_i = R_i/d$ and $r_o = R_o/d$, respectively. The boundary conditions in the axial direction are $\mathbf{u}(r, \theta, \pm 0.5\Gamma, t) = (0, 0, 0)$.

We solve Eq. (1) by using the standard second-order time-splitting method with consistent boundary conditions for the pressure [16]. Spatial discretization is done via a Galerkin-Fourier expansion in θ and Chebyshev collocation in r and z . The idealized boundary conditions are discontinuous at the junctions where the stationary end walls meet the rotating inner cylinder. In experiments there are small but finite gaps at these junctions where the azimuthal velocity is adjusted to zero. To achieve accuracy associated with the spectral method, a regularization of the discontinuous boundary conditions is implemented, which is of the form

$$u_\theta(r, \theta, \pm 0.5\Gamma, t) = \text{Re}\{\exp([r_i - r]/\epsilon) + \exp([r - r_o]/\epsilon)\}, \quad (3)$$

where ϵ is a small parameter characterizing the physical gaps. We use $\epsilon = 6 \times 10^{-3}$. Our numerical method was previously developed to study the end-wall effects in the Taylor-Couette system with co- and counter-rotating cylinders [17, 18]. In the present work we use up to $n_r = 50$ and $n_z = 500$ Chebyshev modes in the radial and axial directions, respectively, and up to $n_\theta = 100$ Fourier modes in the azimuthal direction. The time step is chosen to be $\delta t = 10^{-6}$.

B. Qualitative description of basic dynamical states

1. Low-order instabilities

In the wide-gap Taylor-Couette system various flow patterns and their bifurcation behaviors are relatively well understood [3, 6]. In our narrow-gap setting, the background flow is a number of known low-order, nonturbulent instabilities upon which a new type of ring bursting structures emerges. Here we describe these low-order instabilities. To visualize and distinguish qualitatively different flow patterns, we use the contour plots of the azimuthal vorticity component η .

a. Primary instability: Taylor vortex flow. As the Reynolds number Re is increased, the basic state, circular Couette flow (CCF) becomes unstable and is replaced by the classical Taylor vortex flow (TVF) that consists of toroidally closed vortices. TVFs with increasing numbers of vortices appear gradually over a large range of Re , starting from a single Taylor vortex cell generated through the mechanism of Ekman pumping near the end walls. This initial cell can appear either near the top or the bottom lid. In an ideal system, initial Taylor vortex cells can occur simultaneously at both lids, but this is less likely in realistic systems due to the inevitable imperfections in the system. The onset of initial TVF cells was experimentally found for Re about 358 [10]. We find, numerically, that the onset value is about 356. As Re is increased from this value, additional vortices appear, which enter the bulk from near the lids until they finally fill the whole annulus for Re near 435 (experimentally the value is about 437 [10]). For example, we observe a TVF with 22 pairs of vortices within the annulus, with the characterizing wave number of $k = 3.427$, and an additional pair of Ekman boundary layer vortices near the top and bottom lids. Note that, since the system is finite, Ekman-vortex regions are typically present near the boundaries of the system. In the following we focus on the bulk region that is free of Ekman vortices.

b. Secondary instabilities: Wavy vortex flow. Upon further increase in Re , the TVF becomes unstable and is replaced by a wavy vortex flow (WVF) driven by the axial shear in the azimuthal velocity [19] due to the radial advection of high and low azimuthal momentum close to the inner and outer cylinder, respectively. We find that the onset of WVF occurs for $\text{Re} \approx 473$ (experimentally the value is about 475 [10]). The WVF, as shown in Fig. 1(a), is associated with relatively high values of the azimuthal wave number m . For example, the WVF pattern in Fig. 1(a) has azimuthal wave number $m = 39$, which we call WVF₃₉. We find that this particular WVF state is in fact a global background flow over a wide range of Re values.

The TVF and WVF patterns occur regardless of whether the system has a wide or a narrow gap, although the critical values of Re for the onset of these flow patterns depend on the system details.

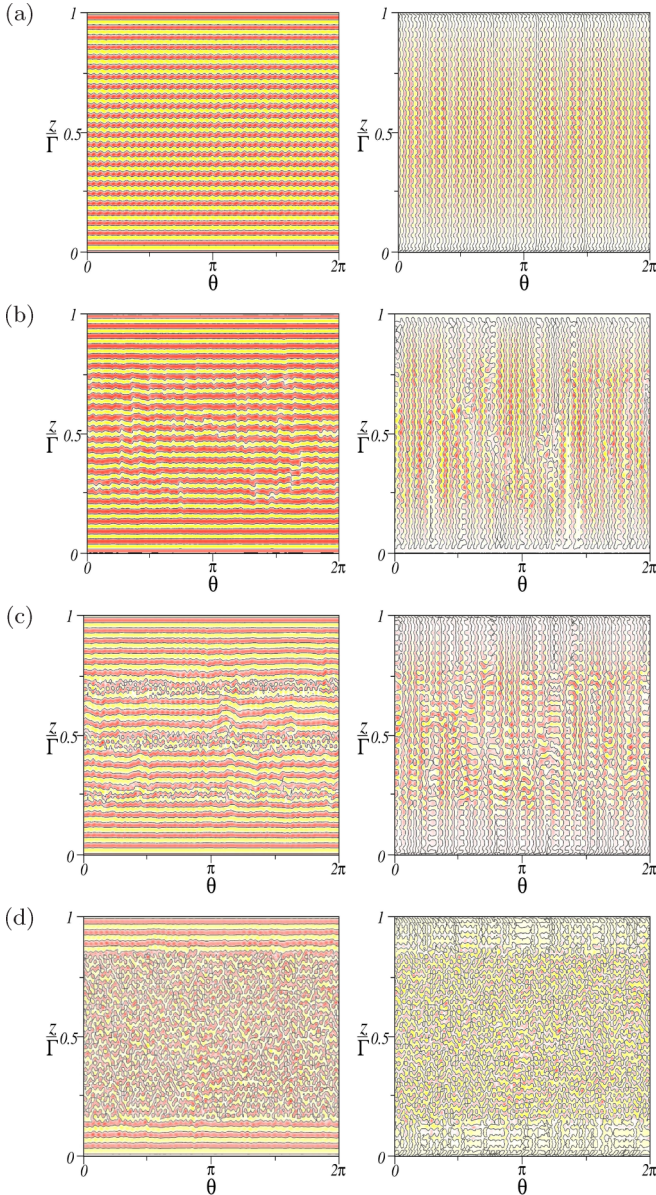


FIG. 1. (Color online) Distinct flow patterns in narrow-gap Taylor-Couette system. Contours of the azimuthal vorticity component η with (left column, $\eta \in [-400, 400]$) and without (right column, $\eta(m \neq 0) \in [-200, 200]$) the axisymmetric component on an unrolled cylindrical surface at the midgap ($r = d/2$) for different flows and different values of Re . Red (dark gray) and yellow (light gray) colors correspond to positive and negative values, respectively, and the black curves indicate the zero contours. Distinct flow patterns are shown in (a) WVF_{39} for $Re = 500$, (b) LP for $Re = 540$, (c) ring bursts ($n = 3$) for $Re = 545$, and (d) VSWB for $Re = 800$, respectively. Note that (d) shows the situation in which VSWBs occupy the entire angular (see Carey *et al.* [10]).

2. High-order instabilities

a. Very short wavelength bursts and localized patches. For the commonly studied [6], wide-gap Taylor-Couette system, e.g., of radius ratio 0.883, the typical sequence of solutions with increasing Re values is as follows. As the stationary TVF becomes unstable, a time-dependent WVF arises, followed

by a modulated WVF [6], eventually leading to turbulent behaviors. However, in the narrow-gap case we do not observe the global transition from WVF to modulated WVF. Instead, we find that a state, named VSWB [10], appears immediately after the onset of WVF *without* any other types of intermediate solutions. The onset of VSWBs occurs for $Re \approx 483$, which agrees with the experimentally observed onset value. The VSWB state can effectively be regarded as a burst because it occurs on top of some background flow structure such as wavy vortices. The term “short wavelength” is with respect to the length scale of the background pattern. VSWB is in fact a state of weak turbulence.

As Re is increased further, we observe *localized patches* (LPs) [10,20] superposed on the WVF. The pattern within LPs can be either wavylike [Fig. 1(b)] or turbulent, depending on the Re value. In particular, wavylike patterns occur for relatively low values of Re but turbulence occurs for high Re values, e.g., for $Re > 580$. A turbulent pattern can either evolve into VSWBs or decay slowly. The number of LPs depends on Re as well. In general, the higher the value of Re the larger the number of LPs that appear, and their lifetimes increase as well. The patches are randomly distributed over the whole bulk length.

b. Ring-bursting patterns. When Re is increased above about 540, we discover a *new* type of localized, intermittent bursting solution, the *ring bursts* that coexist with VSWBs. While both types of solutions are localized, there are characteristic differences. For example, VSWBs appear randomly over the whole bulk fluid region with seemingly expanding behaviors in all directions, but ring bursts always remain *localized* in the axial direction. In fact, the bursts are generated from the localized turbulent patches that grow in the azimuthal direction as Re is increased. For sufficiently high values of Re , the patches extend over one circumference, generating distinct ring bursts that are separated from the flow patterns in the rest of the bulk, as shown in Fig. 1(c). The characteristics of the background flows in the regions surrounding the ring bursts depend strongly on Re . They can range from wavylike patterns (i.e., WVF_{39}) to interpenetrating spirals [6] due to the interactions among various azimuthal wave numbers, as shown in Fig. 1(b). We observe ring-bursting patterns of different order j , as shown in Figs. 1 and 3. For example, we observe ring bursts with larger j values increases with Re . Along the axial direction, the ring-bursting patterns can appear at any position, except for the Ekman-vortex region near the lids, because strong boundary layer vortices prevent the development of ring-bursting patterns. In terms of the lifetime, the ring-bursting patterns exhibit a similar behavior to LPs. In general, the higher the value of Re the longer the lifetime of the pattern, and the lifetime does not seem to depend on the number of ring bursts (order-1, order-2, or order-3).

While there is no apparent order associated with the flow patterns within the ring bursts, the flow in the regions in between exhibit a clear WVF_{39} signature. The ring bursts can spontaneously break up and disappear. Depending on the number of ring bursts, the transient time for the burst to decay into localized patches can be relatively long. In addition, there can be transitions between patterns with distinct numbers of ring bursts. For example, suppose there is a ring-bursting

pattern of order-3. If one ring disappears, a new ring-bursting region can appear and grow. Transitions between patterns with either increasing or decreasing numbers of ring bursts have been observed.

For $Re > 850$, we find that VSWBs can fill the whole bulk fluid region, as shown in Fig. 1(d). For this relatively high Reynolds number, there is one large VSWB pattern that fills the whole annulus. To see the evolution of VSWBs we refer to Fig. 3 in Carey *et al.* [10]. In fact, for $Re > 900$, the entire fluid region is saturated with VSWBs. These numerical observations are in agreement with experimental findings [10].

c. Underlying flow patterns. The right panels in Fig. 1 show contours for the same pattern as those for the left panels but *without* the underlying axisymmetric contribution. The resulting “reduced” flow pattern of WVF_{39} in Fig. 1(a) appears quite regular, indicating the existence of the dominant wavy with azimuthal wave number $m = 39$. The nearly vertical black curves specify the contours of zero vorticity. At several azimuthal positions, these lines narrow, signifying the emergence of a second, but weaker, azimuthal wave number, e.g., $m = 8$. For order-3 ring bursts, the flow patterns near the lids are somewhat modified due to the presence of higher azimuthal wave number m , as shown in Fig. 1(c), where these wave numbers can be seen from the $\eta(m \neq 0)$ plot (right column). The somewhat random patterns near the lids indicate the higher values of the azimuthal wave number m . The flow patterns in the central region (including that containing the three ring bursts) exhibit completely different behaviors. In particular, with respect to the contours $\eta(m \neq 0)$ (right column in Fig. 1) the turbulent ring bursts and the separating WVF_{39} pattern appear *indistinguishable*, suggesting an axisymmetric dominance of the ring bursts. For turbulent flows or VSWBs in Fig. 1(d), none of the patterns has such an ordered structure. The somewhat visible separation by vertical lines in the contours $\eta(m \neq 0)$ for WVF_{39} and order-3 ring bursts [Figs. 1(a) and 1(c)] suggests a similarity to the underlying or surrounding wavylike pattern. However, the contours $\eta(m \neq 0)$ for VSWB [Fig. 1(d)] differ considerably, suggesting that the underlying structure differs. It is in fact turbulent. The schematic diagram in Fig. 2 shows the regimes of Re values in which different flow patterns exist. Regimes on top of each other indicate coexistence and the numbers below the axis give numerical and experimental (in parentheses) values of regime onset, respectively. Note that the thick (solid) dashed line illustrates the regime of LPs with a wavylike or a turbulent interior.

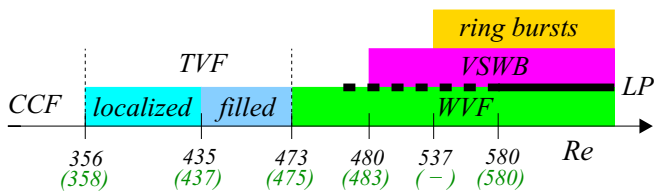


FIG. 2. (Color online) Schematic illustration of the Re regimes in which different patterns exist. Shown are the regimes of CCF, TVF, WVF, and VSWB and ring bursts and their corresponding numerical and experimental (in parentheses) onsets. Thick dashed (solid) line illustrates approximately the existence of LPs with a wavylike or a turbulent interior.

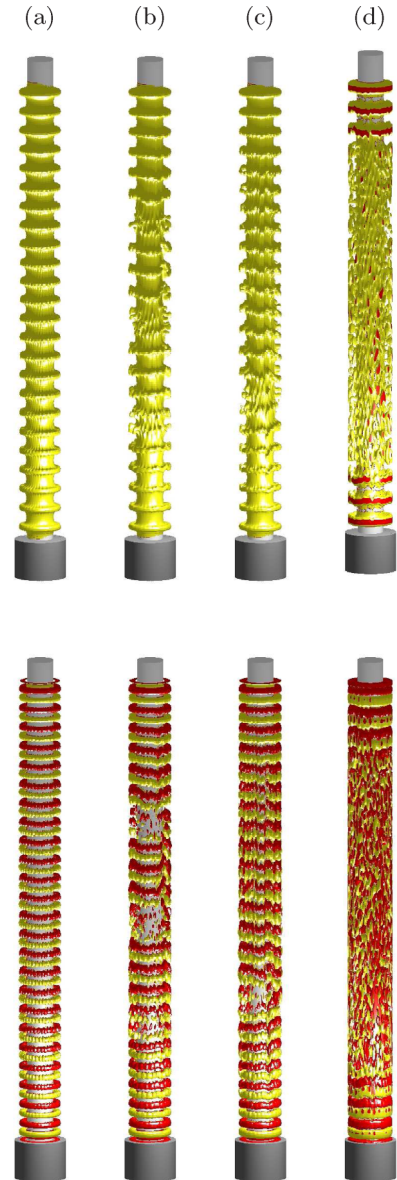


FIG. 3. (Color online) Angular momentum and vorticity. Isosurfaces of rv (top row) and η (bottom row) for flows at different values of Re (isolevels shown for the top and bottom rows are $rv = 80$ and $\eta = \pm 30$, respectively). Red (dark gray) and yellow (light gray) colors correspond to positive and negative values, respectively. The different flow states are shown in (a) WVF_{39} for $Re = 500$, (b) ring bursts (order-3) for $Re = 545$, (c) ring burst (order-1) for $Re = 550$, and (d) VSWB for $Re = 900$, respectively. For clear visualization, here and in all subsequent three-dimensional plots the radius ratio is scaled with the factor 100.

III. CHARACTERIZATION OF RING BURSTS

A. Angular momentum, azimuthal vorticity, and modal kinetic energy

Figure 3 shows the isosurfaces of the angular momentum rv (top row) and azimuthal vorticity η (bottom row) for representative flow patterns at different values of Re . WVF_{39} with the dominant axisymmetric contribution and high azimuthal wave number, as shown in Fig. 3(a), serves

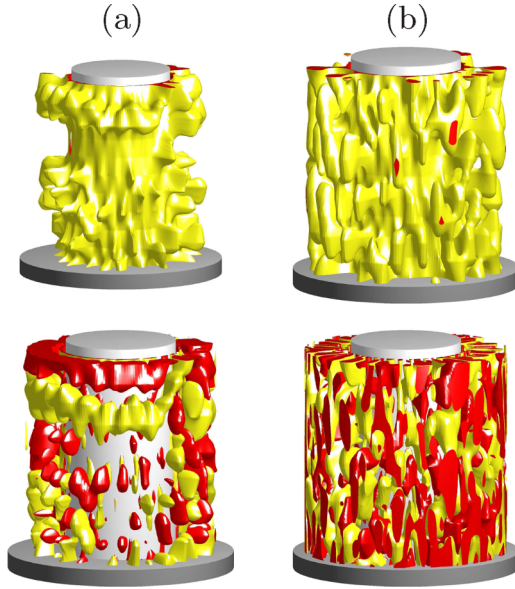


FIG. 4. (Color online) Three-dimensional views of angular momentum and vorticity. Magnitude of the angular momentum (top panels) and azimuthal vorticity (bottom panels) for a flow segment of vertical length $\Gamma/10$ for ring bursts (left column) and VSWB (right column); (a) ring bursts of order-3 for $Re = 545$ and (b) VSWB for $Re = 800$, respectively. The segment is taken from the region containing the middle ring burst in Fig. 3(b) and has the same color coding.

as the background pattern for ring bursts and VSWBs. The three turbulent, azimuthally closed bursting regions associated with the order-3 ring-bursting pattern are distinctly visible, as shown in Fig. 3(b). Within each bursting region, both rv and η appear random but the (background) flow patterns between the bursting regions are remnants of the WVF_{39} pattern. With increasing Re , higher wave numbers emerge, but the separation between bursting and nonbursting regions persists. For high values of Re , VSWBs arise, as shown in Fig. 3(d). In this case, isosurface plots of rv and η exhibit random flow patterns.

To better visualize and illustrate the similarity and differences between ring burst and VSWB patterns, we present in Fig. 4 the angular momentum (top panels) and azimuthal vorticity (bottom panels) for a segment of the bulk flow. The length of the segment is $\Gamma/10$. The entire structure of the ring-bursting pattern possesses an axial symmetry and an azimuthal dominance of rotation symmetric mode ($m = 0$). The interior of the bursting regions has no symmetry—similarly to the structures of VSWBs. There are thus two distinct spatial scales associated with ring bursts: a large scale determined by the azimuthal symmetry and a small scale present in the interior of the bursting regions.

Figure 5 illustrates the time evolution of different ring-bursting patterns. Starting from WVF_{39} at $t = 0$, a ring-bursting pattern emerges almost immediately near the central region ($z/\Gamma \approx 0.5$), followed at $t \approx 0.1$ by the occurrence of an order-2 pattern in the upper half of the bulk ($z/\Gamma \approx 0.7$). For $t \gtrsim 3.5$, an order-3 ring-bursting pattern is formed in the lower half of the bulk ($z/\Gamma \approx 0.25$), which remains in the system for $t \approx 12.5$ and then decays. Hereafter the system shows again an order-2 ring bursting, as the lowest ring burst

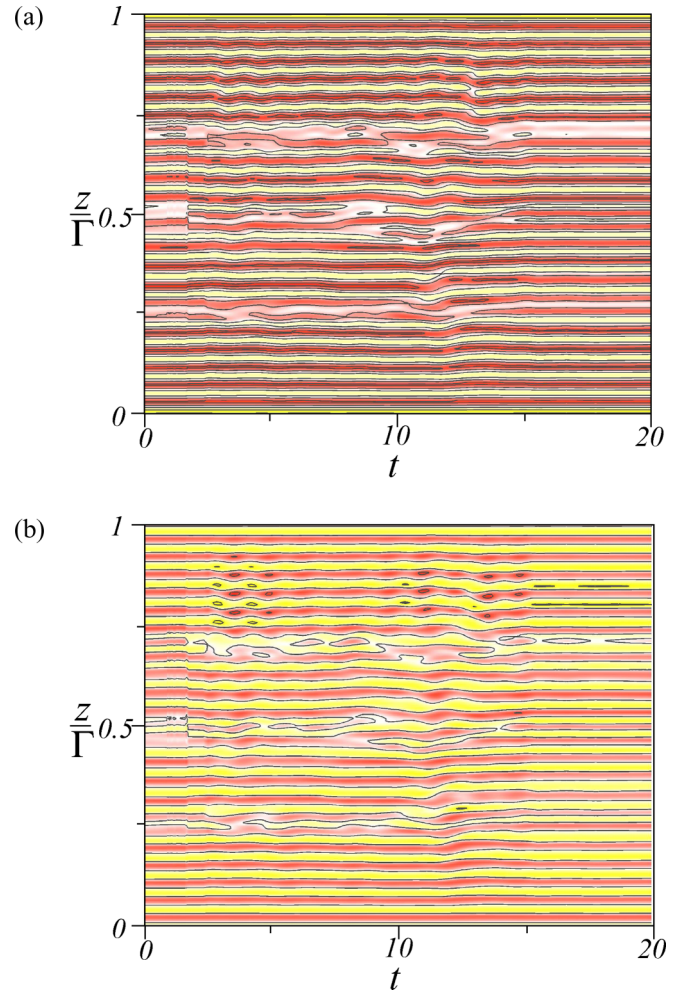


FIG. 5. (Color online) Time series from ring-bursting regime. Time evolution of (a) u_r and (b) η at $\theta = \text{const}$ and midgap of the bulk ($r = d/2$) for a flow exhibiting different ring-bursting patterns (Color coding as in Fig. 1).

region ($z = 0.25z/\Gamma$) has vanished. This pattern persists until $t \approx 15$, at which the order-2 bursting ring disappears with the burst region in the center ($z = 0.5z/\Gamma$). In the time interval considered, an order-1 pattern persists.

Figures 6(a) and 6(b) show the power spectral density (PSD) of the radial velocity profile at the midgap for WVF and ring burst, respectively. We see that the PSD associated with the ring-bursting pattern (b) indicates the existence of significantly higher azimuthal wave number than the WVF pattern (a). In fact, the PSD of WVF_{39} in (a) shows a strong peak at frequency about 19, which corresponds to the dominant azimuthal wave number ($m = 39$). This peak is still present in (b) but it is broadened, indicating WVF as the background flow pattern for the ring burst. Figure 6(c) shows the scaled PSD curves for several flow patterns for different values of Re . We see that the PSD curves for the ring-bursting patterns essentially collapse into one frequency band, but the PSD curve associated with WVF_{39} lies slightly below those of ring-bursting patterns. There is relatively large difference for small frequencies but it becomes insignificant for higher frequencies. This is further support for the role of WVF_{39} in providing the skeleton structure for all ring-bursting patterns.

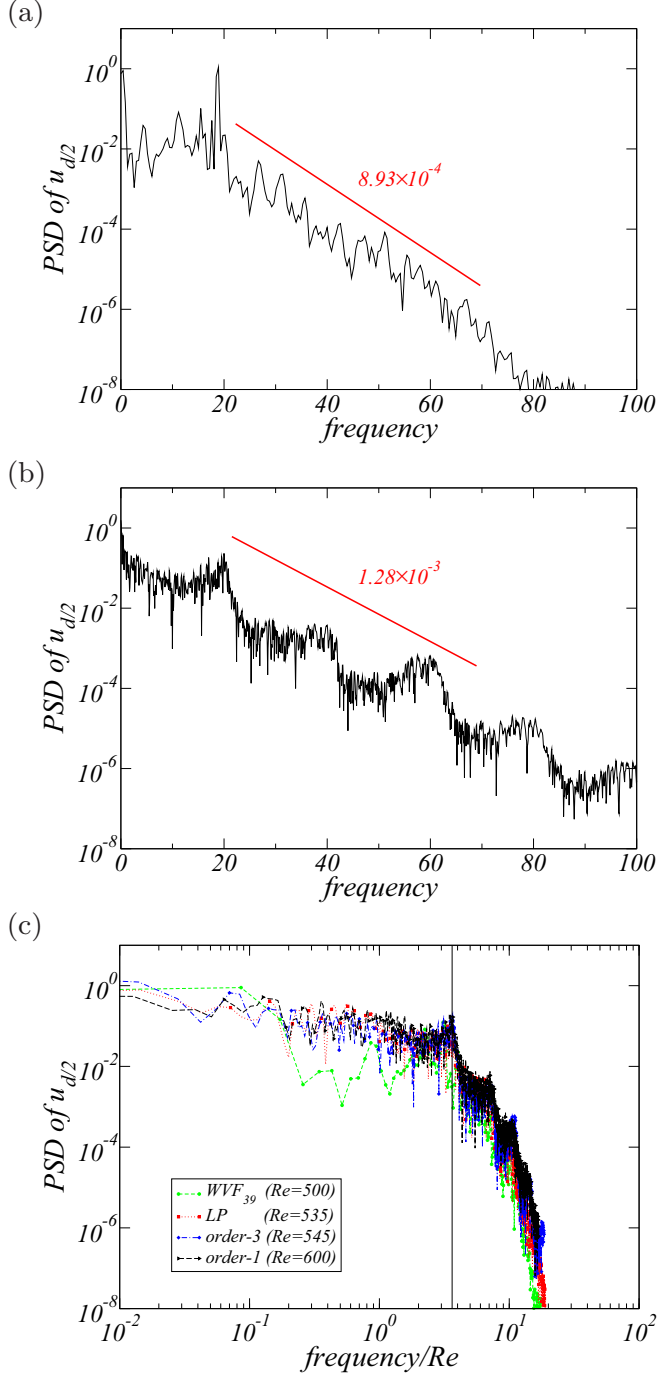


FIG. 6. (Color online) Power spectral density (PSD). PSD curves calculated from the radial flow component $u_{d/2} = u(d/2, 0, \Gamma/2, t)$ for (a) WVF_{39} for $Re = 500$ and (b) ring burst of order-3 for $Re = 545$. (c) PSD curves scaled by the respective Reynolds number for different flow patterns. As the number of ring bursts is increased, the local peaks in the PSD curves become more pronounced. The vertical line highlights the resemblance of the spectra.

B. Cross-flow energy

A suitable and commonly used quantity in the study of fluid turbulence is the cross-flow energy [21], where small values indicate a laminar flow but large values correspond to turbulence.

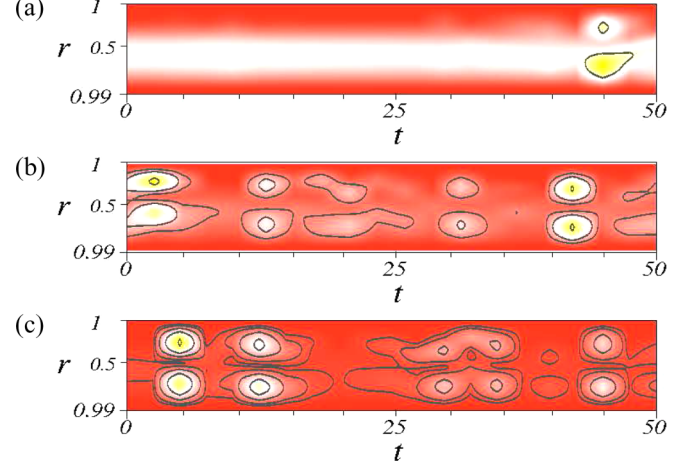


FIG. 7. (Color online) Radial component of cross-flow energy. Space-time plots of the radial component of the cross-flow energy, $E^{cf,r}(r,t) = \langle u_r^2 + u_z^2 \rangle_{A(r)}$, averaged over the surfaces A of a concentric cylinder of radius r for (a) $Re = 500$, (b) $Re = 545$, and (c) $Re = 560$. Red (dark gray) [yellow (light gray)] color indicates high (low) energy value with contours defined as $\Delta E^{cf,r} = 5 \times 10^5$. The maximum energy values in (a)–(c) are approximately 8.1×10^5 , 8.5×10^6 , and 1.2×10^6 , respectively. For better visualization the radial gap width is magnified by the factor of 500 (the same for Fig. 8 below).

1. Radial component of cross-flow energy

The radial component of the cross-flow energy is given by [21]

$$E^{cf,r}(r,t) = \langle u_r^2 + u_z^2 \rangle_{A(r)}, \quad (4)$$

where $\langle \cdot \rangle_{A(r)}$ denotes the average over the surface of a concentric cylinder at radius r . The cross-flow energy component $E^{cf,r}(r,t)$ measures the instantaneous energy associated with the radial and axial velocity components at radial distance r . Figure 7 shows the space-time plots of $E^{cf,r}(r,t)$ over the time period of 50 diffusion times for three values of Re . We observe the temporal emergence and disappearance of various ring-bursting patterns in the bulk. For example, for $Re = 545$, an order-3 ring-bursting pattern exists for $40 \lesssim t \lesssim 44$, and an order-2 pattern appears for $0.5 \lesssim t \lesssim 4.5$, as shown in Fig. 7(b). For $Re = 560$, an order-3 pattern appears for $2.5 \lesssim t \lesssim 7.0$, and a single ring-bursting pattern (order-1) exists for $43 \lesssim t \lesssim 47$, as shown in Fig. 7(c).

Plots of the cross-flow energy exhibit two features. First, the presence of the order-1 ring-bursting pattern is accompanied by a significant increase in the radial cross-flow energy as compared with that associated with the background flow, e.g., WVF_{39} , indicated as the uniform red (dark gray) regions. Second, the profile of $E^{cf,r}(r,t)$ for any ring-bursting pattern is approximately symmetric with respect to the middle of the gap. Regarding the structural properties the ring-bursting patterns are similar to the *turbulent WVF* state [14,22–24] (see Sec. III C). The (radial) symmetry is a consequence of the narrow-gap nature of the flow. From Fig. 7, we see that it is not feasible to determine the number of ring bursts (e.g., order-1, order-2, or order-3) present in the bulk. However, in all cases, this can be done using the magnitude of the cross-flow energy.

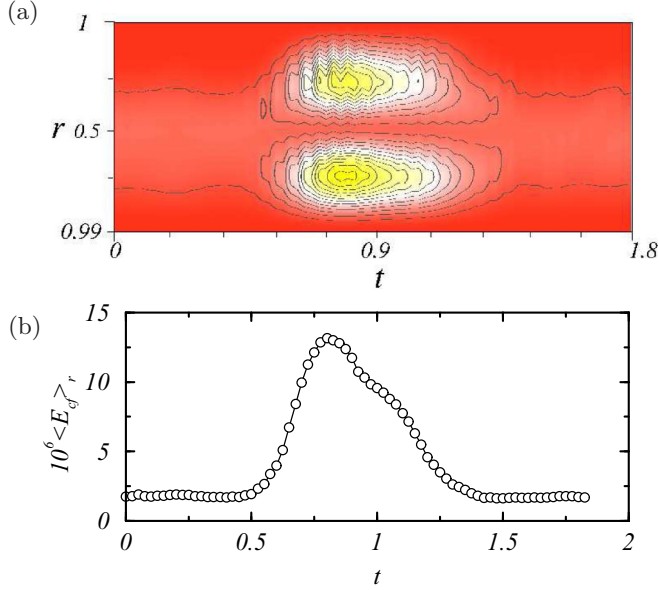


FIG. 8. (Color online) Magnified view of the radial component of the cross-flow energy. (a) Magnification of a segment of Fig. 7(b) for $t \in [0, 1.8]$ illustrating the emergence and disappearance of the order-3 ring-bursting pattern for $Re = 545$ (color coding as in Fig. 7). The contours are defined through $\Delta E^{cf,r} = 5 \times 10^5$, and the maximum energy value is about 8.288×10^6 . (b) Average radial cross-flow energy $\langle E^{cf,r} \rangle_r$ versus t for the order-3 ring burst for $Re = 545$. The nearly constant background flow is WVF₃₉ with $\langle E^{cf,r}(\text{WVF}_{39}) \rangle_r \approx 2 \times 10^{-6}$.

Figure 8(a) shows a magnification of a segment of Fig. 7(b) for $t \in [0, 1.8]$, which contains the emergence and disappearance of an order-3 ring burst for $Re = 545$, occurring at $t \approx 0.45$ and $t \approx 1.35$, respectively. Outside this time interval the flow is WVF₃₉, which constitutes a nearly uniform background without any significant variations in $E^{cf,r}(r, t)$. The spatial distribution of $E^{cf,r}(r, t)$ exhibits an approximate symmetry about $r = 0.5$. Figure 8(b) shows the average cross-flow energy, $\langle E^{cf,r} \rangle_r$, as a function of time t , corresponding to the emergence and disappearance of the ring-bursting pattern. We observe a significant enhancement of the average radial energy over that of the background flow ($\langle E^{cf,r} \rangle_r \approx 2 \times 10^{-6}$). In fact, in the time interval where the ring burst exists, the maximum value of the average radial energy is about one order of magnitude larger than that of the background flow. In general, the maximum energy depends on the number j (order) of ring bursts in the annulus, where a larger value of j corresponds to a higher value of the maximum energy.

The emergence and development of any type of bursting pattern with increasing Re can be conveniently characterized using the quantity f_B , the percentage of the annulus containing bursts in the space-time plot. Figure 9(a) shows f_B versus Re , where we observe approximately a linear behavior for $Re \lesssim 900$, and the transition to bursts occurs for $Re \approx 480$, in agreement with the experimentally found onset of VSWB [10]. Onset of ring bursts can be revealed through examination of the maximum value of the average radial energy $\langle E^{cf,r} \rangle_r$ versus Re , as shown in Fig. 9(b). Regardless of the order of the ring bursts, there is a linear increase in $\langle E^{cf,r} \rangle_r$ with Re ,

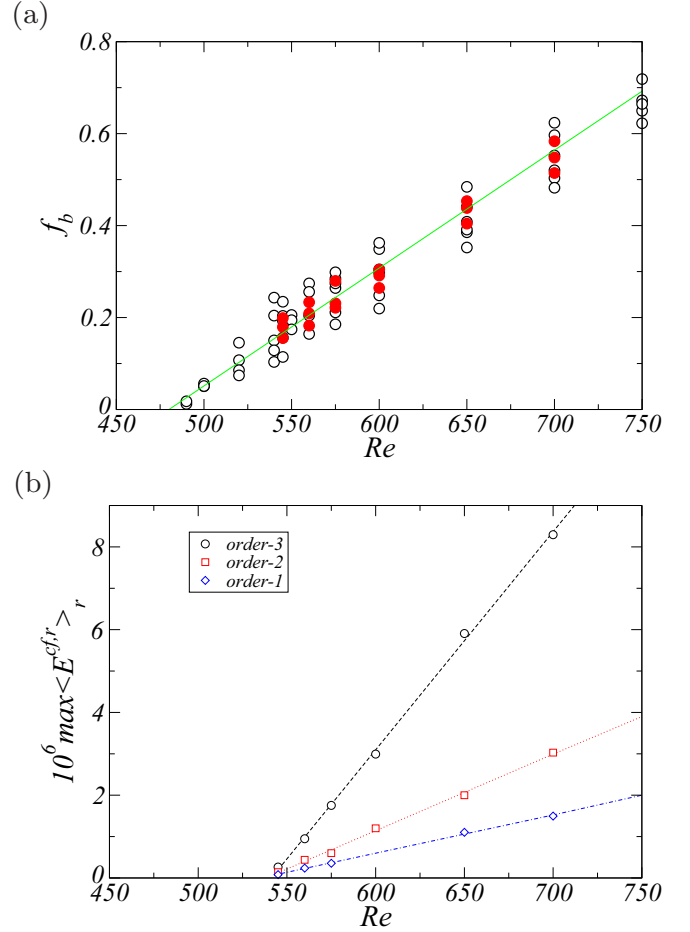


FIG. 9. (Color online) Onset of bursting patterns. (a) Burst fraction f_b as a function of Re . A linear fit indicates that the onset of VSWBs occurs for $Re \approx 480$ (the experimental onset [10] is $Re \approx 483$). (b) The maximum average radial energy $\langle E^{cf,r} \rangle_r$ [Eq. (4)] versus Re for ring bursts of different orders ($j \in \{1, 2, 3\}$). The linear behavior indicates that the ring bursts are a result of a forward bifurcation, the onset of which occurs for $Re_c \approx 537$. In (b), the average energy of the underlying background flow, $\langle E^{cf,r} \rangle_r$, has been subtracted off.

suggesting a type of forward bifurcation. Calculations of the flow amplitudes show a square-root type of scaling behavior with increasing parameter difference from the “critical” point, providing further support for the forward nature of the bifurcation. Due to strong localization, the slope of the linear scaling regime depends on the order of the ring burst. Nonetheless, the onset value $Re_c \approx 537$ of ring bursts does not depend on the order. Thus ring bursts emerge *after* VSWBs ($Re \approx 483$).

2. Axial component of cross-flow energy

The axial component of the cross-flow energy is

$$E_m^{cf,z}(z, t) = \langle (u_r)_m^2 + (u_z)_m^2 \rangle_{A(z)}, \quad (5)$$

where $A(z)$ stands for averaging over the radial and azimuthal variables on the surface of a disk at a fixed axial position z . Figure 10 shows the time-averaged value for the

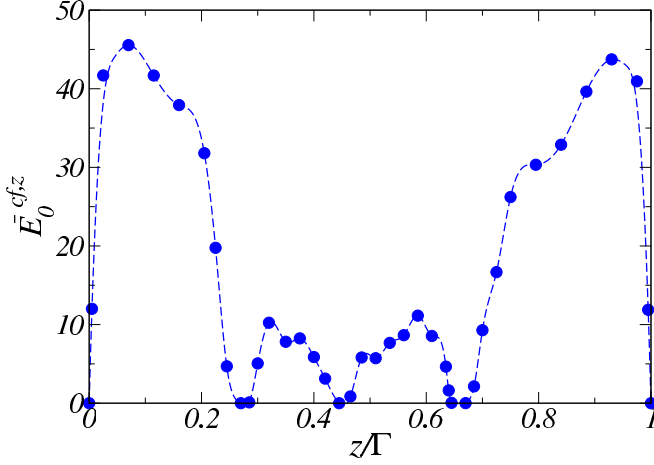


FIG. 10. (Color online) Axial component of cross-flow energy. Associated with the order-3 ring-bursting pattern for $\text{Re} = 545$, time averaged axisymmetric energy component $\bar{E}_0^{cf,z}$. Note that all higher azimuthal wave numbers are on the order of 10^{-4} .

dominant axisymmetric component $\bar{E}_0^{cf,z}$. Near the center of the ring-bursting region in the axial direction, the values of $\bar{E}_0^{cf,z}$ are smaller than those around the edges. However, the contributions from all higher azimuthal wave numbers (not shown), i.e., $\bar{E}_m^{cf,z}$ for $m > 0$, have similarly small magnitudes as compared with $\bar{E}_0^{cf,z}$, which are on the order of 10^{-4} . In fact, for higher azimuthal wave numbers m , the axial components of their cross-flow energies are randomly distributed over z and they are not indicators of any appreciable difference between the background flow and the ring-bursting pattern.

3. Azimuthal wave number separation of axial cross-flow energy

To better characterize the ring-bursting patterns in relation to the background wavylike and general bursting patterns, we devise a method based on the idea of wave number separation. Since a bursting pattern includes modes of higher azimuthal wave numbers, we can decompose the axial component of the cross-flow energy $E_m^{cf,z}(z, t)$ into two distinct subcomponents:

$$E_w^{cf,z}(z) + E_b^{cf,z}(z) = \sum_{m=1}^{m_c-1} E_m^{cf,z}(z) + \sum_{m=m_c}^M E_m^{cf,z}(z), \quad (6)$$

where $E_w^{cf,z}(z)$ and $E_b^{cf,z}(z)$ denote the axial components of the cross-flow energy associated with the background wavylike and burst patterns, respectively, and m_c is some cutoff wave number. Note that the axisymmetric component of the cross-flow energy is excluded because it is significantly larger than all other components (Fig. 10). We choose the normalization factor to be the total cross-flow energy for all azimuthal wave numbers except $m = 0$:

$$E_M^{cf,z}(z) = \sum_{m=1}^M E_m^{cf,z}(z). \quad (7)$$

Figure 11(a) shows the basic E_w and the burst contribution E_b at different axial positions versus the cut-off wave number m_c . We observe that the curves for the z positions within

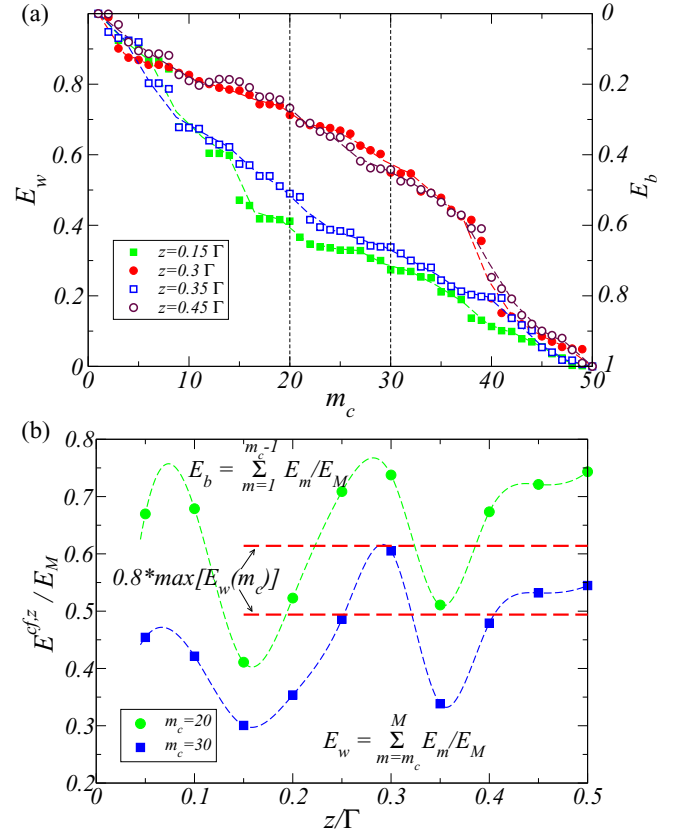


FIG. 11. (Color online) Characterization of axial cross-flow energy based on wave number separation. (a) Variation of the axial cross-flow energy component $E_m^{cf,z}(z) = E_b^{cf,z}(z) + E_w^{cf,z}(z)$ versus the cutoff wave number m_c for two axial positions in the burst region ($z = 0.3\Gamma$ and 0.45Γ , circles) and in the background region ($z = 0.15\Gamma$ and 0.35Γ , squares). (b) Spatial variations of $E_b^{cf,z}(z) = \sum_{m=1}^{m_c-1} E_m^{cf,z}(z)$ and $E_w^{cf,z}(z) = \sum_{m=m_c}^M E_m^{cf,z}(z)$ with z for $m_c = 20$ (circles) and 30 (squares), respectively. Regions above (below) each curve indicate E_b (E_w). The two horizontal dashed lines give the 80% threshold of the maximum values of $[E_w(m_c = 20)]$ (lower) and $[E_w(m_c = 30)]$ (upper), respectively. In the calculations the zero wave number contribution is excluded. Due to normalization with E_M the sum must be unity.

the bursting region [in Fig. 11(a) at $z = 0.3\Gamma$ and 0.45Γ] are higher than those in the wavylike background [in Fig. 11(a) at $z = 0.15\Gamma$ and 0.35Γ], where the former exhibit a rapid decrease in the energy to collapse with the latter for m_c about 39. The variations of E_b and E_w along the annulus length for two different cutoff wave numbers [$m_c = 20, 30$, as indicated by the vertical lines in Fig. 11(a)] are shown in Fig. 11(b). Neglecting the differences in their magnitudes, the variations show qualitatively similar behaviors. Using a cutoff level at 80% of the maximum of the background contribution $E_w(m_c)$, we find a good agreement with the visible energy thresholds between the background and burst regions (cf. Fig. 1). We thus see that, through a proper choice of the cutoff wave number, the bursting and nonbursting regions can be distinguished by examining the axial cross-flow energy variations associated with the cutoff wave number.

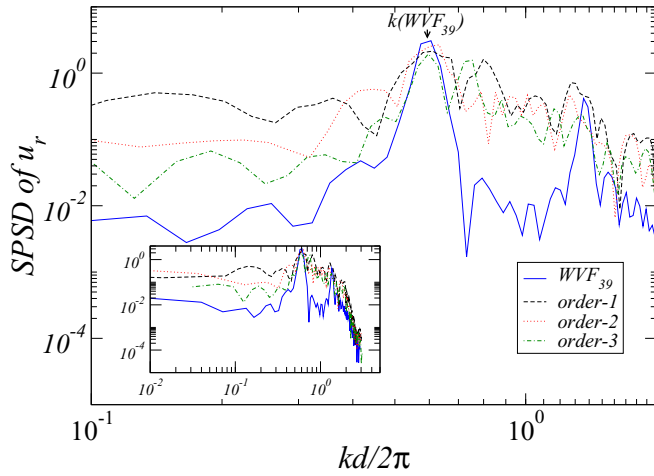


FIG. 12. (Color online) Spatial power spectral density (SPSD) of the radial velocity u_r at the midgap for $Re = 545$, where k is the axial wave number. Inset shows the full spectrum.

C. Axial spacing and localization

The axial ranges of distinct ring-bursting regions are approximately identical. Figure 12 shows the spatial power spectral density (SPSD) of the radial velocity u_r along a line at the midgap in the center of the bulk for the background flow and three types of ring-bursting patterns. Here SPSP is a power spectral density obtained from an axial Fourier transformation. In particular, we use a window of 0.8Γ about the center of the system for the axial Fourier transform to avoid the Ekman regions near the lids. We observe that the four curves coincide at the first sharp peak determined by the wave number associated with the background flow WVF_{39} that consists of 24 vortex pairs in the axial direction. The corresponding axial wavelength and wave number are $\lambda \approx 1.667$ and $k \approx 3.770$, respectively. In addition, several broadband peaks at higher wave numbers exist in the SPSP of the ring-bursting patterns, corresponding to a number of short wavelength bursts within the respective patterns. The broadband nature at higher wave numbers is indicative of the dominance of small-scale bursting patterns. The axial spacing is apparently independent of the value of Re and of the order of the ring-bursting pattern. The typical value of axial expansion agrees well with the axial dimension of two-pair Taylor vortices that constitute four single vortex cells, which holds for all ring-bursting flows that we have succeeded in uncovering. Analogous to the behavior of the cross-flow energy, this behavior is indicative of turbulent WVFs [14,22–24]. We note that the size of only one pair of Taylor vortices (two cells) is too small to account for the observed range of axial expansion. This is consistent with the formation process of ring bursts. In particular, any localized turbulent patch, after its generation, first expands in the axial direction (to four cells) before growing in the azimuthal direction. Whenever the bursting region has expanded to a larger size in the axial direction, the closed ring structure is destroyed, leading to VSWBs.

IV. CONCLUSIONS AND DISCUSSIONS

This paper provides a comprehensive numerical study of the Taylor-Couette system of radius ratio 0.99 and stationary

outer cylinder, a regime that was not studied previously. The relevant control or bifurcation parameter is the Reynolds number Re . For small Re values, TVF initially arises near one of the lids in a single cell, extends, and, finally, fills the bulk interior completely. As Re is increased the TVF loses its stability and WVF emerges through a supercritical Hopf bifurcation. WVFs with high azimuthal wave numbers, e.g., $m = 39$, constitute a persistent background flow, on top of which more complex flow structures develop, such as VSWBs that have been experimentally observed [10].

The main result of this paper is the uncovering of a new type of transient, intermittent state *en route* to turbulence with increasing Re : ring bursts. They emerge when localized turbulent patches grow and close azimuthally, signifying a higher-order instability. The ring bursts occur in various orders and the azimuthally closed bursting regions possess axially expanding subregions surrounded by the WVF background flow or more complex flows at high Re values. The ring-bursting patterns differ characteristically from the localized VSWB turbulent patches. The axial expansion of ring-bursting patterns of different orders correlates well with the size of the double-pair Taylor vortex structure, providing a plausible reason for the similarity of the patterns to the turbulent WVF structure [14,22–24] that usually occurs in the whole annulus at higher Reynolds numbers. We develop a wave number separation method based on decomposing the cross-flow energy to distinguish bursting and nonbursting patterns. In particular, the burst regions are associated with high order and the nonbursting regions (background flow) are associated with lower order azimuthal wave numbers. We also find that the radial cross-flow energy changes significantly in the presence of ring-bursting patterns. By examining the maximum value of the cross-flow energy, we determine the onset of the ring-bursting patterns at the critical Reynolds number of $Re_c \approx 537$, which is larger than that for the onset of VSWBs [10] (about 482). For ring-bursting patterns of different orders, their expansions in the axial direction are nearly identical, and they tend to shift along the axial direction.

There are a number of differences between turbulence in the wide-gap (e.g., radius ratio 0.5 to 0.8) and narrow-gap (e.g., radius ratio 0.99) Taylor-Couette systems. First, in the wide-gap case, the intensity distributions of turbulent fluctuations are often uneven in the radial direction [14,21], where more energetic turbulent fluctuations occur towards the inner cylinder wall. The regions near the inner cylinder thus exhibits stronger turbulence than in the region near the outer cylinder. This radial dependence of turbulent fluctuations is lost in the narrow-gap Taylor-Couette system, where turbulence is observed through the bulk in the radial direction. Second, in wide-gap systems, phenomena such as turbulent streaks [14], small-scale Görtler vortices, and herringbone-like streaks [15] can occur near both inner and outer cylindrical walls. Examining the typical size of the small Görtler vortices [15] reveals that, in the narrow-gap case these vortices have expansion larger than the radial width, excluding the possibility of generating turbulent streaks from small-scale Görtler vortices. Indeed, our simulations do not reveal any small-scale vortices. This might explain the loss of radial dependence of turbulence, as can be seen, e.g., from the cross-flow energy behavior in Fig. 7. In fact, in narrow-gap systems turbulence emerges at the boundary layer

of the neighboring vortex cells almost immediately at any radial position.

While there are ring-bursting patterns of turbulent bands in planar Couette flow systems [25,26], the background flow is quiescent, which defines a threshold between a “simple” state and the coexisting turbulent state. However, in our narrow-gap Taylor-Couette system, the background flow has wavylike patterns, which represents a “threshold” state between an already complex (nonbasic) state and turbulence. Despite these differences there is in fact a remarkable similarity between turbulence in both types of systems. For example, detailed investigations [25] of the separating regime of laminar and turbulent characteristics in planar Couette flows revealed isolated band states of turbulence in confined domains close to the global stability threshold. In the plane Couette flow [25], these bands appear at different angles but are always parallel for a given experiment or simulation. They are remarkably analogous to our ring-bursting patterns on an unrolled cylindrical surface (e.g., comparing Fig. 1 with Fig. 11 in Ref. [26]). In addition, the routes to turbulence are

similar: In both cases the turbulent bands grow out of a small localized turbulent spot that subsequently expands in some direction.

It may be challenging to detect ring-bursting patterns experimentally as they coexist with other complex states such as VSWBs with similar turbulent characteristics. Nonetheless, given that the Taylor-Couette system is a paradigm enabling well-controlled experiments on complex vortex dynamics and turbulence, we are hopeful that our finding will stimulate further research of turbulence in narrow-gap regime of the system, a regime that has received little attention in spite of the large body of literature on Taylor-Couette flows.

ACKNOWLEDGMENTS

Y.D. was supported by Basic Science Research Program through the National Research Foundation of Korea (NRF) funded by the Ministry of Education, Science and Technology (NRF-2013R1A1A2010067). Y.-C. L. was supported by AFOSR under Grant No. FA9550-15-1-0151.

-
- [1] U. Frisch, *Turbulence* (Cambridge University Press, Cambridge, UK, 1996).
 - [2] G. I. Taylor, *Philos. Trans. R. Soc. London A* **223**, 289 (1923).
 - [3] D. Coles, *J. Fluid Mech.* **21**, 385 (1965).
 - [4] H. A. Snyder, *J. Fluid Mech.* **35**, 337 (1969).
 - [5] R. C. DiPrima and H. L. Swinney, *Hydrodynamic Instabilities and the Transition to Turbulence* (Springer, Berlin, 1985), pp. 139–180.
 - [6] C. D. Andereck, S. S. Liu, and H. L. Swinney, *J. Fluid Mech.* **164**, 155 (1986).
 - [7] R. Tagg, *Nonlinear Sci. Today* **4**, 1 (1994).
 - [8] P. Chossat and G. Iooss, *The Couette-Taylor Problem* (Springer, Berlin, 1994).
 - [9] K. Coughlin and P. S. Marcus, *Phys. Rev. Lett.* **77**, 2214 (1996).
 - [10] C. S. Carey, A. B. Schlender, and C. D. Andereck, *Phys. Rev. E* **75**, 016303 (2007).
 - [11] S. Altmeyer and C. Hoffmann, *New J. Phys.* **12**, 113035 (2010).
 - [12] P. R. Fenstermacher, H. L. Swinney, and J. P. Gollub, *J. Fluid Mech.* **94**, 103 (1979).
 - [13] P. W. Colovas and C. D. Andereck, *Phys. Rev. E* **55**, 2736 (1997).
 - [14] S. Dong, *J. Fluid Mech.* **587**, 373 (2007).
 - [15] H. Görtler, ACA Tech. Memo. 1375 (1954).
 - [16] S. Hughes and A. Randriamampianina, *Int. J. Heat Fluid Flow* **28**, 501 (1998).
 - [17] M. Avila, M. Grimes, J. M. Lopez, and F. Marques, *Phys. Fluids* **20**, 104104 (2008).
 - [18] S. Altmeyer, Y. Do, F. Marques, and J. M. Lopez, *Phys. Rev. E* **86**, 046316 (2012).
 - [19] D. Martinand and E. Serre, and R. Lueptow, *Phys. Fluids* **26**, 094102 (2014).
 - [20] S. Ciliberto and P. Bigazzi, *Phys. Rev. Lett.* **60**, 286 (1988).
 - [21] H. J. Brauckmann and B. Eckhardt, *Phys. Rev. E* **87**, 033004 (2013).
 - [22] Y. Tseng and J. Ferziger, *J. Turbulence* **5**, 1 (2004).
 - [23] N. Ohmura, T. Makino, A. Motomura, Y. Shibata, and K. Kataoka, *Int. J. Heat Fluid Flow* **19**, 159 (1998).
 - [24] S. Dong, *Phys. Rev. E* **77**, 035301(R) (2008).
 - [25] D. Barkley and L. S. Tuckerman, *Phys. Rev. Lett.* **94**, 014502 (2005).
 - [26] L. S. Tuckerman and D. Barkley, *Phys. Fluids* **23**, 041301 (2011).